Phase diagram of quantum Hall breakdown and nonlinear phenomena for InGaAs/InP quantum wells

V. Yu,[1,2] M. Hilke,[1,*] P. J. Poole,[2] S. Studenikin,[2] and D. G. Austing[1,2,†]
[1]*Department of Physics, McGill University, Montréal, Quebec, Canada H3A 2T8*
[2]*Emerging Technology Division, National Research Council of Canada, M50, 1200 Montreal Road, Ottawa, Ontario K1A 0R6, Canada*

(Received 29 March 2018; revised manuscript received 15 June 2018; published 24 October 2018)

We investigate nonlinear magnetotransport in a Hall bar device made from a strained InGaAs/InP quantum well: a material system with attractive spintronic properties. From extensive maps of the longitudinal differential resistance (r_{xx}) as a function of current and magnetic (B) field, phase diagrams are generated for quantum Hall breakdown in the strong quantum Hall regime reaching filling factor $\nu = 1$. By careful illumination, the electron sheet density (n) is incremented in small steps and this provides insight into how the transport characteristics evolve with n. We explore in depth the energetics of integer quantum Hall breakdown and provide a simple picture for the principal features in the r_{xx} maps. A simple tunneling model that captures a number of the characteristic features is introduced. We present results on the quantum Hall transport diamonds, a spin-flip resonance at high current near $\nu = 1$, instabilities at large B field and current, and a zero-current anomaly. In addition, parameters such as critical Hall electric fields and the exchange-enhanced g factors for odd-filling factors including $\nu = 1$ are extracted. A detailed examination is made of the B-field dependence of the critical current as determined by two different methods and compiled for different values of n. A simple rescaling procedure that allows the critical current data points obtained from r_{xx} maxima for even filling to collapse onto a single curve is demonstrated. Exchange-enhanced g factors for odd filling are extracted from the compiled data and are compared to those determined by conventional thermal-activation measurements. The exchange-enhanced g factor is found to increase with decreasing n.

DOI: 10.1103/PhysRevB.98.165434

I. INTRODUCTION

The quantum Hall effect occurs in a two-dimensional electron gas (2DEG) confined in a quantum well (QW) when subjected to a high perpendicular magnetic field [1]. By passing a sufficiently high current through a Hall bar, the quantum Hall effect can be destroyed [2]. Current-induced quantum Hall breakdown is a valuable tool to access nonlinear magnetotransport phenomena in a 2DEG (see the extensive review in Ref. [3] and references therein). Some examples of the rich variety of nonlinear phenomena that can be accessed in a strong magnetic field at and beyond current-induced quantum Hall breakdown include the following: hysteresis arising from dynamic nuclear polarization through the interplay of electron and nuclear spins via the hyperfine interaction near integer odd-filling factors [4,5], cyclotron emission at terahertz frequency arising from nonequilibrium electron distribution in Landau levels [6,7], electric instability leading to resistance fluctuations and negative differential resistance [8–11], and reentrant quantum Hall states of the second Landau level [12,13].

The above-mentioned phenomena are typically observed in widely studied GaAs/AlGaAs heterostructure 2DEGs with high mobility. Here we report on the general characteristics of quantum Hall breakdown in an InGaAs/InP QW Hall bar device. Such indium-based QWs are of current interest for spintronic applications. As compared to widely employed GaAs/AlGaAs QWs, InGaAs/InP QWs offer larger electron g factors, stronger spin-orbit coupling, and the nuclear spin for indium (9/2) is larger than for gallium (3/2) [14–20]. We examine in detail two-dimensional maps of the differential resistance as a function of current and magnetic field. These maps may be regarded as phase diagrams and provide a wealth of information about quantum Hall breakdown (including the conditions for, and the energetics of, quantum Hall breakdown), and a number of other rarely studied phenomena for sheet current densities up to $\sim$1 A/m. We describe how quantum Hall breakdown and nonlinear phenomena evolve systematically not only with increasing magnetic field (B) up to 9 T (equivalently decreasing filling factor ν) but also with increasing electron sheet density from 1.6×10^{11} cm^{-2} up to 3.9×10^{11} cm^{-2}. The capability to increment the electron density in small steps by careful illumination was particularly valuable and enabled us to compile sufficient data to examine, for example, trends in electronic g factors and to compare different methods by which the breakdown current can be extracted. In contrast to an earlier study of an InGaAs/InP QW in Ref. [21], here we access the strong quantum Hall regime ($\nu = 1$). We note that there are some reports of current-induced breakdown in other indium-based QW systems where $\nu = 1$ is also attained (see Ref. [22] for InGaAs/InAlAs QWs and Ref. [23] for InSb/AlInSb QWs).

The outline of this paper is as follows. Section II describes details of the InGaAs/InP heterostructure and the Hall bar

*hilke@physics.mcgill.ca
†guy.austing@nrc-cnrc.gc.ca

investigated, and transport characteristics of the 2DEG as a function of the electron density. Section III explains how differential resistance color maps are generated and outlines the principal features that are revealed. Section IV describes how the breakdown characteristics evolve with electron density. Section V provides a simple picture for the principal features in the differential resistance color maps and introduces a simple tunneling model that captures a number of characteristic features. Section VI describes parameters that can be extracted from the transport diamonds in the strong quantum Hall regime: principally, the critical Hall electric fields for $\nu = 1$ and $\nu = 2$ and an estimate of the g factor for $\nu = 1$. Section VII examines in detail the B-field dependence of the critical breakdown current as determined by two different methods compiled for different electron densities. The g factors for odd-filling factors extracted from the compiled data are compared to those determined by conventional thermal-activation measurements. Lastly, Sec. VIII discusses a curious and as yet unexplained zero-current anomaly readily visible in the experimental data over a wide B-field range.

II. EXPERIMENTAL DETAILS AND 2DEG CHARACTERISTICS

The investigated 2DEG is formed in the QW region of a strained $In_{0.76}Ga_{0.24}As/In_{0.53}Ga_{0.47}As/InP$ heterostructure grown by chemical beam epitaxy. The conducting channel in the QW is an undoped 10 nm $In_{0.76}Ga_{0.24}As$ layer. As compared to lattice matched $In_{0.53}Ga_{0.47}As/InP$ QWs, the 0.76 indium fraction is intended to reduce the effective mass and maximize the mobility at the cost of introducing strain [24]. Because of the mobility enhancement, $In_xGa_{1-x}As$ QWs with In fraction x of ~0.75 have attracted attention over the years [25–33]. Other details of the growth and heterostructure are given in Refs. [21,34]. All the transport measurements described in this report are for a 15 -μm-wide Hall bar prepared by standard optical lithography and wet etching [34]. Three pairs of potential probes separated by 50 μm are positioned along the Hall bar and the potential probes have width 7.5 μm where they join the Hall bar. The Hall bar is ~200 μm long and opens out at either end to avoid sharp corners on the entry to the source and drain regions. The Hall bar device design and dimensions were motivated by the work in Refs. [4,5]. Soldered indium beads that are subsequently annealed at 350 °C in vacuum for 30 mins form Ohmic contacts. The device is maintained at the base temperature of a top-loading ^{3}He Janis cryostat equipped with a 9 T superconducting magnet.

Before discussing the nonlinear transport measurements, we describe the standard characteristics of the 2DEG. As an alternative approach to changing the electron sheet density (n) by applying a voltage to a front or back gate, we could controllably increment n in small steps from ~0.5 to ~4.0×10^{11} cm^{-2} by careful illumination of the Hall bar at ~0.3 K with a standard red-light-emitting diode passing a small current up to a few tens of nanoamperes. Figure 1 shows the 0.3 K values of n and (transport) mobility μ obtained using a standard lock-in technique with ac excitation current of 100 nA at 13.5 Hz. We note that here, n is the Hall carrier density. Data points were collected on three separate cooldowns. The dependence of mobility on electron density

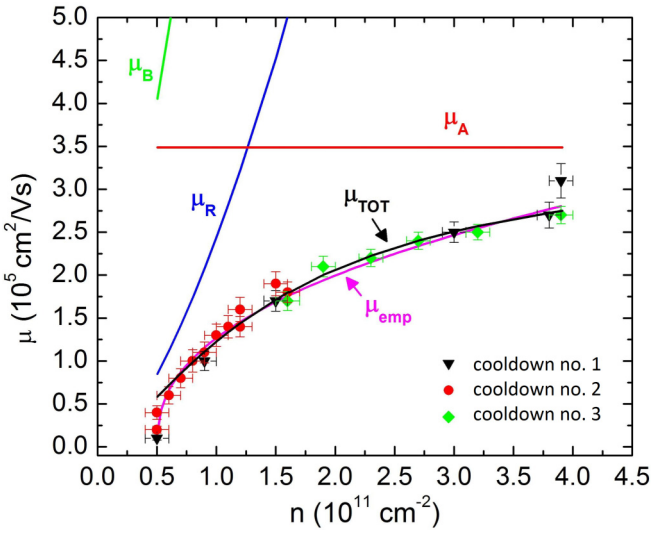

FIG. 1. 0.3 K values of electron density n and mobility μ attained by illumination over three separate cooldowns nos. 1–3. Estimated uncertainties in n and μ are included for each data point. Empirically, over the accessible density range, we find that the mobility follows a power-law dependence $\mu_{emp} \sim (n - n_0)^p$, where $n_0 = 0.50 \pm 0.02 \times 10^{11}$ cm^{-2} and $p = 0.42 \pm 0.02$ (see dashed magenta trace). Following the model in Ref. [35], we have also fitted our data for ionized impurity scattering and short-range alloy disorder scattering. Included in the figure are the calculated mobility vs density traces for background ionized impurity scattering (μ_B: green trace), remote ionized impurity scattering (μ_R: blue trace), short-range alloy disorder scattering (μ_A: red trace), and the total mobility [$\mu_{tot} = (\mu_B^{-1} + \mu_R^{-1} + \mu_A^{-1})^{-1}$: black trace] [36]. For the fits, we excluded the anomalous outlying point near 4.0×10^{11} cm^{-2}.

is reproducible from cooldown to cooldown except near the highest density, ~4.0×10^{11} cm^{-2}, attained for maximum illumination that leads to saturation of the persistent photoconductivity effect [37]. We note that $n = 4.0 \times 10^{11}$ cm^{-2} is well below the electron density required to populate the first-excited subband of the QW (estimated to be 1.8×10^{12} cm^{-2} based on a simple calculation using appropriate material parameters). Empirically, we find that the observed sublinear dependence of mobility on electron density follows a power-law relationship, $\mu_{emp} \sim (n - n_0)^{0.42}$, where n_0 is a constant; see magenta trace in Fig. 1. The observed dependence is qualitatively similar to those reported in earlier works on InGaAs QWs (see, for example, Refs. [27,37,38]). The dependence is consistent with theoretical models for disorder scattering mechanisms in 2DEG structures [35,38]. At low electron density, μ is expected to increase with n when limited by ionized impurity scattering. At high electron density, μ is expected to saturate in quantum wells [39] (or even decrease with n in heterojunctions [40]), when limited by alloy disorder scattering. Following the model in Ref. [35] which includes screening, we have fitted our data incorporating the appropriate scattering mechanisms. Figure 1 includes calculated mobility versus density traces for background ionized impurity scattering (μ_B), remote ionized impurity scattering (μ_R), short-range alloy disorder scattering (μ_A), and the total mobility $\mu_{tot} = (\mu_B^{-1} + \mu_R^{-1} + \mu_A^{-1})^{-1}$ [36].

For the experiments discussed below, we focus on data taken during the third cooldown (no. 3) for which n is in the range 1.6–3.9 $\times 10^{11}$ cm^{-2}. Over this range, from the determined values of the transport mobility, we find that the transport mean free path (transport lifetime) increases from 1.2 μm (4.8 ps) to 2.7 μm (7.1 ps). For the transport lifetime, we took the effective mass (m^*) to be $0.047m_0$, where m_0 is the free-electron mass [21]. From other measurements (data not shown [34]), we also determined the quantum mobility μ_q and, subsequently, the quantum lifetime τ_q by Dingle plot analysis of the low B-field Shubnikov–de Haas (SdH) envelope [21,41]. μ_q (τ_q) is found to be ∼12 000 cm^2/Vs (∼0.31 ps) for n in the range 1.6–3.2 $\times 10^{11}$ cm^{-2}, but rises to ∼19 000 cm^2/Vs (∼0.51 ps) near 3.9 $\times 10^{11}$ cm^{-2} when the electron density is close to saturating. From τ_q, we can then estimate the Landau- level broadening Γ. Defining the full width at half maximum (FWHM) of a Lorentzian-shaped Landau level to be 2Γ [21], we find $2\Gamma = \hbar/\tau_q$ to be in the range ∼1.2–2.0 meV. Note that for this Hall bar, the longitudinal resistance becomes very large at low density, $n = n_0 \sim 0.5 \times 10^{11}$ cm^{-2}, when the 2DEG is almost insulating and the mobility collapses (see Fig. 1). This density (marking the percolation threshold for transport) equates to a Fermi energy of ∼2 meV. From this observation, we conclude that there are effective random potential fluctuations of amplitude ∼2 meV.

III. DIFFERENTIAL RESISTANCE COLOR MAPS

A map (or "phase diagram") displaying how the nonlinear transport properties of quantum Hall breakdown depend on current (I) and B field can be built up by sweeping the current and stepping the B field. Color maps of directly measured as opposed to numerically derived longitudinal and transverse differential resistances r_{xx} and r_{xy}, respectively, are shown in Fig. 2 for $n = 1.6 \times 10^{11}$ cm^{-2}. The four-point measurements of the differential resistances, $r_{xx}(I_{dc}) \equiv dV_{xx}/dI$ and $r_{xy}(I_{dc}) \equiv dV_{xy}/dI$, were performed simultaneously by driving a combination of a dc current I_{dc} and a small ac excitation current of 100 nA at 13.5 Hz through the Hall bar and measuring the ac voltage component drop ΔV_{xx} and ΔV_{xy} between appropriate potential probes of the Hall bar using a standard lock-in technique [21,42].

The distinctive dark-blue diamond-shaped regions in the map of r_{xx} identify where $r_{xx} \sim 0$. These regions are the so-called transport diamonds [21]. In the map of r_{xy} too, diamonds are visible within which the r_{xy} is quantized. The diamonds in r_{xx} and r_{xy} occupy the same region in the I-B plane. We can now assign these transport diamonds to specific integer filling factors from the value of r_{xy} consistent with the expected quantized values of the Hall resistance. We conclude that the two most prominent diamonds centered at 3 and 6 T in Fig. 2 are related to filling factors $\nu = 2$ and 1, respectively.

We note the following about the transport diamonds revealed in Fig. 2: (i) a horizontal cut through the diamonds in r_{xx} near $I_{dc} \sim 0$ would essentially give a traditional plot of $R_{xx} = V_{xx}/I_{dc}$ with swept B field when measured in the low current linear response regime ($R_{xx} = r_{xx}$) and reveals zeros in R_{xx} at integer filling factors at high B field in the quantum Hall regime and SdH minima at low B field; (ii) with increasing B field, the diamonds become more pronounced and bigger (most clearly reflected in the maximum width in the current of the diamonds); (iii) on passing from inside a diamond to outside a diamond, the quantum Hall effect breaks down; and (iv) beyond the diamonds, the quantum Hall effect has broken down and transport is generally nonlinear ($R_{xx} \neq r_{xx}$).

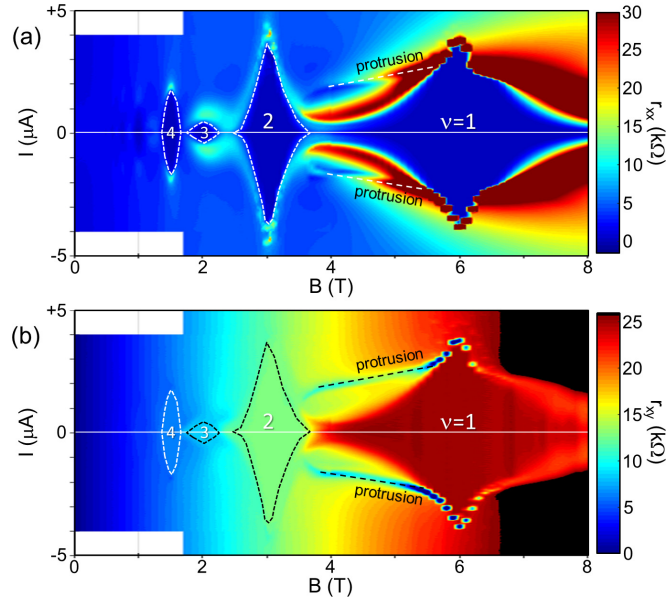

FIG. 2. Experimental color maps of (a) r_{xx} and (b) r_{xy}: $n = 1.6 \times 10^{11}$ cm^{-2}, $\mu = 170\,000$ cm^2/Vs. Note that the regions of r_{xy} exceeding 26 kΩ are colored black. In both panels, the $\nu = 2$, 3, and 4 transport diamonds are outlined, and the high-current protrusion features emerging from near the high current tips of the $\nu = 1$ transport diamond are identified. The color maps are built up with three overlying data sets. The current sweep rate is typically a few tens of nanoamperes per second. The B-field step at low (high) B field is 25 mT (100 mT).

The color maps provide a wealth of information in the strong quantum Hall regime beyond that reported in Ref. [21], which describes transport diamonds for an InGaAs/InP Hall bar but only for B fields up to 5 T and for $n = 5.3 \times 10^{11}$ cm^{-2}, so filling factors no lower than $\nu = 5$ were investigated. We found it insightful to capture color maps over a wide range of B field and for sheet current densities up to ∼1 A/m. The color maps in Fig. 2 together with those presented in the next section for progressively higher electron density provide access to a wide range of filling-factor diamonds from $\nu = 1$ to at least 10. We note that a color map of V_{xx} showing the $\nu = 2$ diamond is presented in Ref. [43] for a GaAs/AlGaAs Hall bar of width 10 μm, and color maps of differential resistance between $\nu = 2$ and 4 are presented in Refs. [12,13] for high-mobility GaAs/AlGaAs structures of width 500 μm or greater and for sheet current densities much less than 1 A/m.

In particular, with the capability to measure the $\nu = 1$ transport diamond, we uncovered distinctive high-current features that emerge from near the high-current tips of the diamond. These "protrusions" (resonances) are clear in Fig. 2 as peaks in r_{xx} and valleys in r_{xy} that track to lower current

as the B field is reduced, and end near the high B-field side of the $\nu = 2$ diamond. Note that the value of r_{xy} in the valley is $\sim h/2e^2$ or lower. The protrusion features were also seen in a second Hall bar device made from a similar $In_{0.76}Ga_{0.24}As/In_{0.53}Ga_{0.47}As/InP$ heterostructure (data not shown [34]). The protrusions are discussed further in Secs. IV and V.

IV. ELECTRON DENSITY DEPENDENCE OF QUANTUM HALL BREAKDOWN FEATURES

Figure 3 shows measured color maps of r_{xx} for six electron densities from the lowest ($n = 1.6 \times 10^{11}$ cm^{-2}) to the highest ($n = 3.9 \times 10^{11}$ cm^{-2}). Several noteworthy trends are clear with increasing electron density:

(1) The transport diamonds shift systematically to higher B field, as expected. For example, the center of the $\nu = 2$ diamond shifts from $\sim$3 T at $n = 1.6 \times 10^{11}$ cm^{-2} to $\sim$7.5 T at $n = 3.9 \times 10^{11}$ cm^{-2}. Note that the $\nu = 1$ diamond is substantially in range only for the first two densities.

(2) The size of the transport diamonds increases. For example, the maximum critical current of the $\nu = 2$ diamond increases from $\sim 4\ \mu$A at $n = 1.6 \times 10^{11}$ cm^{-2} to $\sim 11\ \mu$A at $n = 3.9 \times 10^{11}$ cm^{-2}. We will return to the subject of how the critical currents for even- and odd-filling factors vary with B field and electron density in Sec. VII.

(3) The phenomenon of phase inversion of SdH oscillations at high-filling factors discussed in Ref. [21] due to electron heating is observed at low B field and high current (see also Ref. [23] for a discussion of electron heating at low B field for InSb/AlInSb QWs), and the phase inversion becomes more visible at higher electron density. By phase inversion, we mean that the minima (maxima) of SdH oscillations in r_{xx} versus B field at zero current develop into maxima (minima) at high current (see also Fig. 4).

(4) High even-filling-factor ($\nu \geqslant 6$) transport diamonds reported in Ref. [21] appeared to have straight edges. This would seem to be the case too in Fig. 3, but closer inspection reveals otherwise for low-filling-factor diamonds. For example, the $\nu = 4$ diamond appears to have straight edges at low density, but these edges become curved at higher density. The edges of the $\nu = 1$ and $\nu = 2$ diamonds are clearly curved for all densities shown [44].

(5) Regarding odd-filling factors, at $n = 1.6 \times 10^{11}$ cm^{-2}, only the $\nu = 1$ transport diamond is well developed. At $n = 3.9 \times 10^{11}$ cm^{-2}, the $\nu = 3$ and $\nu = 5$ diamonds become clear too. The $\nu = 1$ diamond is out of range beyond 9 T.

(6) Outside the $\nu = 1$ transport diamond, features where $r_{xx} \geqslant 10$ kΩ protrude towards lower B field are clear for the lower densities. These protrusions always start from near the finite-current tips of the $\nu = 1$ diamond and appear to track towards zero current at 0 T. They also weaken and eventually terminate at a point located approximately midway along the high B-field sides of the $\nu = 2$ diamond (for example, near 4.3 T for $n = 1.9 \times 10^{11}$ cm^{-2}). We will discuss these protrusions later in Sec. V in connection to Fig. 5.

(7) At higher density, the regions just outside the $\nu = 3$ and $\nu = 5$ transport diamonds develop a distinctive double-peak structure. These double-peak features where $r_{xx} \geqslant 5$ kΩ are clearest at $n = 3.9 \times 10^{11}$ cm^{-2} (in the color map, the peaks are marked by asterisks on the positive current side). For both the $\nu = 3$ and $\nu = 5$ diamonds, the leftmost peak is near the finite-current tip of the diamond and the rightmost peak is located on the high B-field side of the diamond. The origin of the curious double-peak features is unknown.

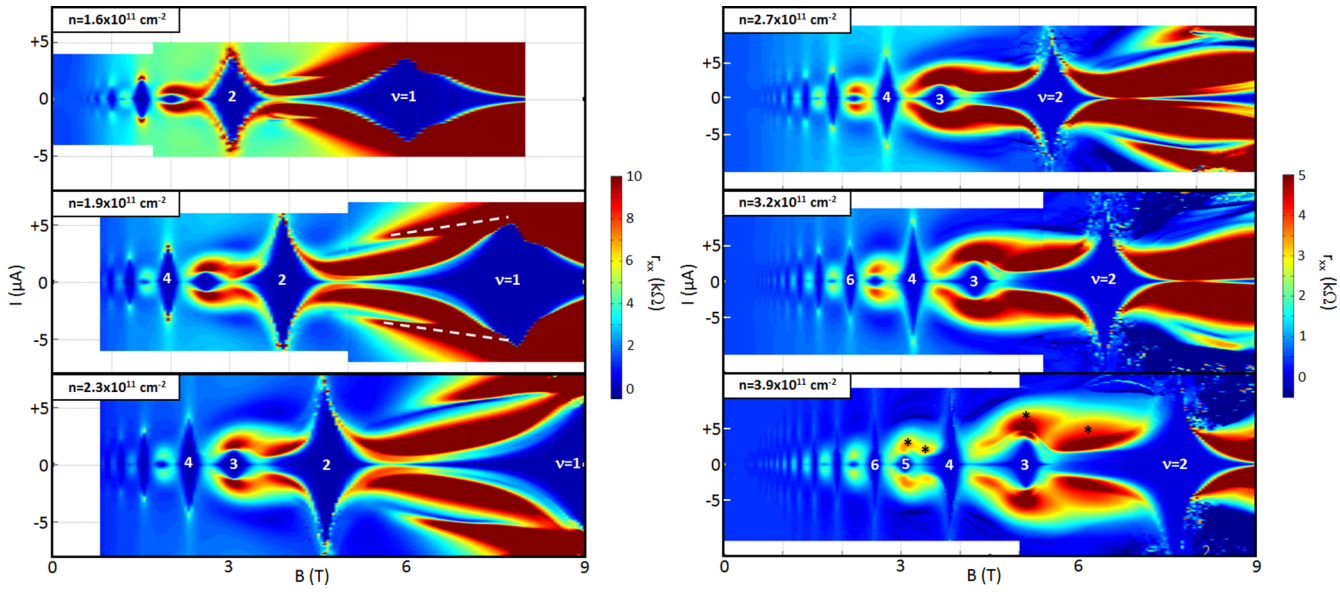

FIG. 3. Experimental color maps of r_{xx} for six electron densities in the range of $n = 1.6 \times 10^{11}$ cm^{-2} to $n = 3.9 \times 10^{11}$ cm^{-2} attained after controlled illumination. Note that for the left- (right-)side panels, the color scales and the current axis ranges are different. White dashed lines through the center of the protrusions are marked on the color map for $n = 1.9 \times 10^{11}$ cm^{-2}. Asterisks identify distinctive "double-peak" features for positive current polarity in the vicinity of the $\nu = 3$ and 5 transport diamonds in the color map for $n = 3.9 \times 10^{11}$ cm^{-2}. The color map for $n = 3.9 \times 10^{11}$ cm^{-2} is replotted in Fig. 4 with a different color scale to highlight certain features more clearly.

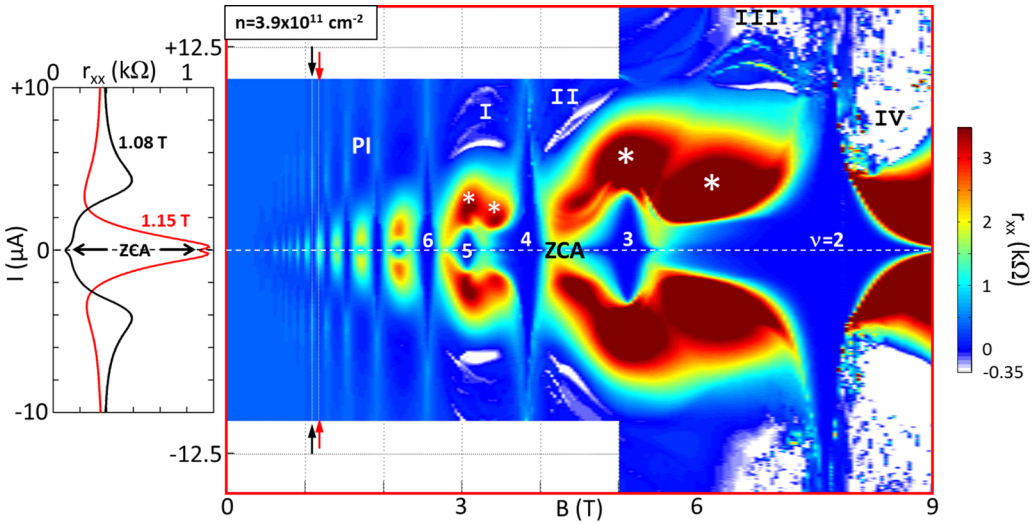

FIG. 4. Color map of r_{xx} for the highest electron density $n = 3.9 \times 10^{11}$ cm^{-2} replotted with a different color scale to emphasize certain features. Phase inversion (PI) of SdH oscillations due to electron heating is observed at low B field (high filling factor). The left panel illustrates the PI effect. The black (red) r_{xx} trace at 1.08 T (1.15 T) cutting through $\nu = 14$ SdH minimum (neighboring SdH maximum) at zero current develops into a maximum (minimum) at ∼4 μA (∼3 μA). The zero-current anomaly (ZCA) "dip," discussed further in Sec. VIII, is also clear in these two traces. Asterisks in the color map identify the distinctive "double-peak" features in the vicinity of the $\nu = 3$ and 5 transport diamonds. Regions exhibiting negative differential resistance appear white ($r_{xx} \leqslant 350\ \Omega$) and become widespread beyond 3 T (see, for example, the crescent-shaped features marked I and II between 3 and 5 T. Concurrently, instability appearing as random "spots" of color also develops above 6 T near the $\nu = 2$ diamond (see region marked III) and becomes very pronounced on the high B-field side of the diamond (see region marked IV).

(8) Starting at $n = 2.7 \times 10^{11}$ cm^{-2}, close inspection of the color maps on the right side of Fig. 3 reveals that outside the transport diamonds (when the quantum Hall effect has broken down), regions appear where: (i) r_{xx} approaches zero or even becomes negative, i.e., negative differential resistance is exhibited, and (ii) r_{xx} is unstable. These features become even more pronounced at higher density. For clarity, in Fig. 4 we have replotted the color map for $n = 3.9 \times 10^{11}$ cm^{-2} with a color scale that enhances these features. Regions appearing white, where $r_{xx} \leqslant 0$, become widespread beyond 3 T, and instability develops near the $\nu = 2$ diamond, especially on the high B-field side (see the random "spots" of color). We will examine these features of electric instability in more detail elsewhere [45].

(9) Although integer filling-factor diamonds are clear in Fig. 3, fractional filling-factor diamonds are not observed even for $n = 3.9 \times 10^{11}$ cm^{-2} when the transport mobility is highest (see Fig. 1). The absence of fractional filling-factor diamonds in our data contrasts with those observed between $\nu = 2$ and 4 in Refs. [12,13] for high-mobility GaAs/AlGaAs heterostructures ($\mu \sim 2 \times 10^7$ cm^2/Vs). Based on a simple Coulomb interaction picture [46,47], we estimate the energy gap for fractional states to be 0.56 meV (0.74 meV) at 4 T (7 T) [48]. However, the disorder strength in the measured InGaAs/InP heterostructure is significant ($\hbar/\tau_q \sim 1.2$–2.0 meV; see Sec. II) and is comparable to or exceeds the estimated energy gap for fractional states. This accounts for the absence of fractions. Moreover, alloy disorder scattering in the $In_{0.76}Ga_{0.24}As$ QW channel is likely even more disruptive to the fractional states [49].

V. SIMPLE PICTURE OF TRANSPORT DIAMONDS

We now present a simple picture of how we interpret key features related to quantum Hall breakdown that appear most clearly in the color maps of r_{xx}. We will use the color map of r_{xx} for $n = 1.9 \times 10^{11}$ cm^{-2} in Fig. 5 for this purpose.

It is nontrivial to directly relate current (y axis in the color maps) to energy: a point that will be emphasized further in Sec. VII. However, two features of the transport diamonds stand out. First, the diamond size generally increases with increasing B field (for odd-filling and even-filling factors separately). Second, the diamond size alternates between relatively small for odd-filling factors and relatively big for even-filling factors. These observations strongly suggest that the width of the diamond in current is related to the Zeeman energy splitting ($|g^*|\mu_B B$) at odd filling and to the cyclotron energy ($\hbar\omega_c = \hbar eB/m^*$) at even filling. Here, g^*, μ_B, $\hbar$, and e, respectively, are the effective g factor, Bohr magneton, reduced Planck constant, and charge of an electron. For odd-filling factors, we would then expect the maximum width of the $(2N + 1)$th diamond ($N = 0, 1, 2, \ldots$ for $\nu = 1, 3, 5, \ldots$) to reflect the transition $(N, \uparrow) \rightarrow (N, \downarrow)$ where the Landau-level index N is conserved, but electron spin is flipped (by hyperfine or spin-orbit coupling [5]) from up to down. For even-filling factors, the maximum width of the $(2N + 2)$th diamond ($N = 0, 1, 2, \ldots$ for $\nu = 2, 4, 6, \ldots$) could reflect the transition $(N, \downarrow) \rightarrow (N + 1, \downarrow)$, where N is changed but electron spin is conserved. More likely, it reflects the lower-energy transition $(N, \downarrow) \rightarrow (N + 1, \uparrow)$ where electron spin is flipped too. This transition has energy $\hbar\omega_c - |g^*|\mu_B B$. In Fig. 5, we have added white guide lines that separately bound

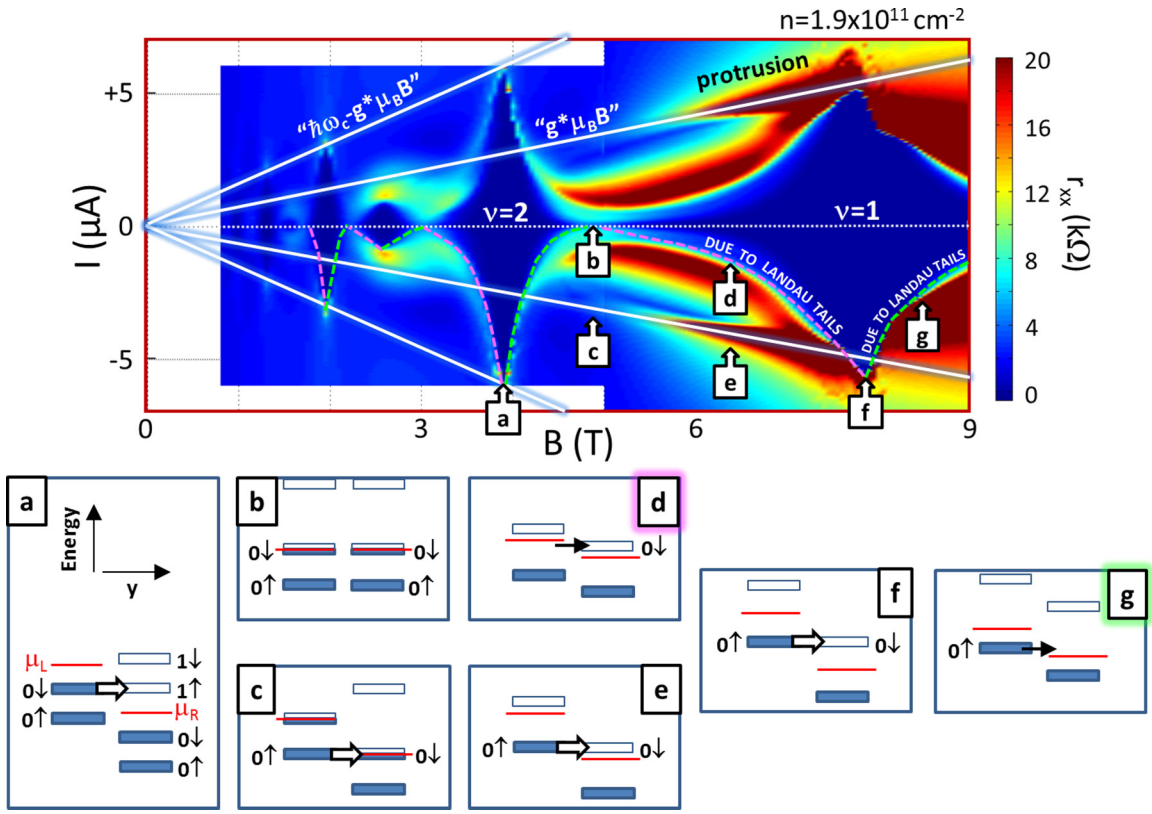

FIG. 5. Experimental color map of r_{xx} for $n = 1.9 \times 10^{11}$ cm^{-2}. White guide lines bounding tips of even- (odd-)filling-factor diamonds are shown and reflect principally the growth in the cyclotron energy (Zeeman energy splitting) with B field. Cartoons (a)–(g) illustrate alignment of Landau levels for the feature marked on the color map. See text for full description.

odd- and even-filling-factor diamonds and interpolate to zero current at zero field. In Sec. VII, we will more carefully examine the magnetic field dependence of the critical currents.

The transitions that we picture as relevant are principally tunneling transitions between Landau levels that are tilted in the y direction (across the Hall bar). These transitions are induced by the Hall electric field when current is applied. This Zener-type tunneling mechanism is discussed in Refs. [50,51]. Inter-Landau-level tunneling is also referred to in the literature as quasielastic inter-Landau-level scattering [50]. Figures 5(a)–5(g) illustrate alignment of spin-split Landau subband energy levels for the features marked on the color map. In each cartoon, there are two ladders of energy levels. Relevant levels are labeled in compact form, for example, $0\uparrow = (0, \uparrow)$. Extended states in each level are shown as bars, and blue (white) identifies filled (empty) states. The left (right) ladder of levels is filled up to the local chemical potential μ_L (μ_R). L and R represent two points along the y axis. L and R are defined such that $\mu_L \geqslant \mu_R$ so that transitions occur from the left ladder to the right ladder for either current polarity. In the next section, we will specify further what points ideally L and R represent and discuss the characteristic length scales that could be associated with the separation between these two points.

The specific features marked in Fig. 5 are the following:

(1) At $\nu = 2$, the chemical potential is midway between $(0,\downarrow)$ and $(1,\uparrow)$. At the tips of the $\nu = 2$ diamond [Fig. 5(a)], breakdown occurs when fully filled $(0,\downarrow)$ at L aligns with empty $(1,\uparrow)$ at R [Fig. 5(a) depicts a resonant inter-Landau-level transition with spin flip]. Similarly, at $\nu = 1$, the chemical potential is midway between $(0,\uparrow)$ and $(0,\downarrow)$. At the tips of the $\nu = 1$ diamond [Fig. 5(f)], breakdown occurs when fully filled $(0,\uparrow)$ at L aligns with empty $(0,\downarrow)$ at R [Fig. 5(f) depicts resonant transition between spin-split subband levels of the $N = 0$ Landau level].

(2) Figure 5(f) also corresponds to the high B-field end of the protrusion. Figures 5(e) and 5(c) depict alignment for points along the protrusion to lower B field for the same $(0,\uparrow) \rightarrow (0, \downarrow)$ resonant transition when μ_R approaches $(0,\downarrow)$ [Fig. 5(e)] and lies through $(0,\downarrow)$ [Fig. 5(c)].

(3) At zero current, the $\nu = 1$ and $\nu = 2$ diamonds touch near 4.9 T [Fig. 5(b)] [52]. For small currents, in the vicinity of the point at Fig. 5(b), intrasubband transitions occur.

(4) Lastly, Figs. 5(d) and 5(g), respectively, represent processes responsible for the edges of the $\nu = 1$ diamond on the low (dashed pink line) and high (dashed green line) B-field side. In both cases, localized states in the Landau-level subband tails are important and the processes occur similarly for the other diamonds. Figure 5(d) depicts transitions from localized states at L in the high- [low]-energy tail of $(0,\uparrow)$ [$(0,\downarrow)$] to extended states in empty $(0,\downarrow)$ at R. Figure 5(g) depicts transitions from extended states in full $(0,\uparrow)$ at L to localized states at R in the high- [low]-energy tail of $(0,\uparrow)$ [$(0,\downarrow)$]: extended states in $(0,\uparrow)$ at L are no longer all filled.

We are not aware of any calculation or model that would substantially reproduce, even qualitatively, many of the notable features in the color map of r_{xx} in Fig. 5 (and color maps in Fig. 3). We have developed a toy model that does

generate a number of general features observed in the experimental color maps. The model is a one-dimensional tunneling model (see the Appendix for further details). The motivation for this approach is that the measured color map in its entirety primarily reflects the B-field evolution of the Landau levels and the broadening of the Landau levels. This is captured by the model. The model though is not microscopic and it does not explicitly include details of spin-flip mechanisms, i.e., all energetically allowed transitions are permitted whether or not electron spin is flipped. The generated color maps are also sensitive to the choice of the form of the density of states (see the Appendix for an example of a color map generated with our model).

VI. TRANSPORT DIAMONDS IN STRONG QUANTUM HALL REGIME

Two metrics are frequently quoted in the literature to characterize breakdown: the critical current density $J_c = I_c/w$ at a given filling factor ν (where I_c and w, respectively, are the critical current and Hall bar width) and the corresponding critical Hall electric field $E_c = hI_c/\nu e^2 w$ (where h is the Planck constant). Although in the following section we will more carefully discuss how one can define and extract I_c, from Fig. 5, we estimate that $I_c \sim 6$ μA ($\sim$5 μA) from the tips of the dark-blue colored $\nu = 2$ ($\nu = 1$) diamond at 3.9 T (7.8 T) for $n = 1.9 \times 10^{11}$ cm^{-2}. Thus, J_c and E_c are, respectively, $\sim$0.4 A/m and $\sim$5.2 kV/m ($\sim$0.33 A/m and $\sim$8.6 kV/m) at $\nu = 2$ ($\nu = 1$). We can compare these numbers with those compiled in Refs. [53,54] for GaAs/AlGaAs 2DEG heterostructures. Interestingly, the numbers we obtain for the InGaAs/InP QW here are quite similar in value. For example, from Refs. [53,54], we infer E_c is in the range of 2–6 kV/m at 4 T ($\sim$6 kV/m at 8 T) for even-filling (odd-filling) factors. In our estimation of J_c and E_c, we took w to be the nominal width of the Hall bar (=15 μm) and neglected any reduction due to wet etching and side-wall depletion.

Assuming the Landau levels are tilted uniformly across the Hall bar, one would anticipate that one could make a crude estimate of the minimum characteristic separation between points L and R (δ in the toy model described in the Appendix) required to induce the transitions depicted in Fig. 5. We shall examine the estimated value for E_c of $\sim$5.2 kV/m at $\nu = 2$ ($B = 3.9$ T) for $n = 1.9 \times 10^{11}$ cm^{-2}. For the pure Zener tunneling mechanism represented in Fig. 5(a), we might expect $E_c \sim \Delta/e\delta$ where $\Delta = \hbar\omega_c - |g^*|\mu_B B$ is evaluated at 3.9 T with appropriate values of $0.047m_0$ and 4.8, respectively, for m^* and $|g^*|$ [55]. Hence, a value for the characteristic length scale $\delta \sim \Delta/eE_c \sim$ (8.5 mV)/(5.2 kV/m) of 1.6 μm is determined. Reasonably, $\delta \ll w = 15$ μm: we would not expect direct tunneling from one side of the Hall bar to the other side. However, δ is two orders of magnitude larger than the distance over which we would expect direct inter-Landau-level tunneling to be significant. As discussed in Ref. [53], the tunneling distance can be related to the spatial extent of wave functions of electrons in the Landau levels. This is comparable to the magnetic length $\ell_B = 25.6\ \text{nm}/\sqrt{B}$, with B in units of Tesla. For $B = 3.9$ T, $\ell_B \sim 13$ nm $\ll \delta$. The values for E_c that we determine experimentally are similar to those reported in the literature for GaAs/AlGaAs 2DEGs and are up to two orders of magnitude smaller than expected based on a simple pure Zener tunneling picture (also see Ref. [51]).

While a fully satisfactory answer to the longstanding problem of accounting for the empirical values of E_c remains to be found [53], we make the following comments. The experimentally derived critical Hall electric fields, equally the critical current densities, should be regarded as *average* quantities across the width of the Hall bar. Furthermore, the Landau levels are not tilted uniformly across the Hall bar. Two effects locally can significantly enhance the electric field. First, the Landau levels bend up strongly near the edges of the Hall bar [43,56,57]. Second, in reality, there are random potential fluctuations in the 2DEG due to disorder [9,58–61]. Lastly, although Zener tunneling is almost certainly involved in quantum Hall breakdown, it is not the only factor. In the electron heating model of Komiyama and Kawaguchi [51], the role of Zener tunneling is primarily to kickstart an avalanche multiplication of excited carriers, the conditions for which depend upon the details of energy balance between gain and loss processes [62].

To finish this section, we describe how the $\nu = 1$ and $\nu = 2$ transport diamonds in Fig. 5 can be used to make a crude estimate of the g factor for $\nu = 1$. $n = 1.9 \times 10^{11}$ cm^{-2} is the highest electron density for which the $\nu = 1$ diamond is substantially visible with the 9 T magnet available in the experiments. Note that the energy gap associated with the $\nu = 1$ diamond is too large for the g factor to be determined by performing thermal-activation measurements over the accessible temperature range of 270 mK to 1.5 K. Instead, we start with the observation that the maximum breakdown current for the $\nu = 2$ diamond is $\sim$6 μA at 3.9 T. We take this current to be proportional to energy $\hbar\omega_c - |g_e^*|\mu_B B \sim 8.5$ meV. The subscript e is to emphasize that the g factor should be that appropriate for an even-filling factor (we have used the value of 4.8 estimated from separate measurements [55]). For the $\nu = 1$ diamond, the maximum breakdown current is $\sim$5 μA at 7.8 T. We take this current to be proportional to energy $|g_o^*|\mu_B B$. The subscript o is to emphasize that the g factor should be that appropriate for an odd-filling factor subject to enhancement by many-body electron-electron exchange interactions [21,63–66]. Assuming the constant of proportionality for converting current to energy is the same for both diamonds, the 5 μA breakdown current for $\nu = 1$ is equated to the energy $\sim$7 meV, implying $|g_o^*| \sim 16$. Our estimation of $|g_o^*|$ here has neglected Landau-level broadening and assumed that the breakdown currents quoted above for the $\nu = 1$ and 2 diamonds reflect the corresponding resonant transitions (effectively, method B to be described in Sec. VII). We will discuss these assumptions further in the following section. Nonetheless, recent calculations of the exchange enhancement of g factors in strained InGaAs/InP heterostructures suggest that values of magnitude exceeding 10 are possible for $\nu = 1$ [66].

VII. B-FIELD DEPENDENCE OF CRITICAL BREAKDOWN CURRENT

The maximum critical current I_c at integer filling (where the transport diamond is widest) and how it depends on the magnetic field with varying electron density have received

considerable attention for a number of decades. Not only has this subject been of interest for metrological reasons, but, in principle, the dependence can shed light on the physical mechanisms that drive quantum Hall breakdown; see, for example, Refs. [3,51,53,54,67]. Controlled illumination allows us to compile sufficient data for different values of n to examine the magnetic field dependence of I_c for even- and odd-filling factors for an InGaAs/InP QW 2DEG: a system other than GaAs/AlGaAs which is usually investigated.

The choice of how one defines the onset of breakdown can influence the value of I_c. The following two methods are reasonable and have been used in the literature. For method A, I_c is taken to be the value at which r_{xx} exceeds a small threshold. The value of the threshold though is influenced to a degree by the noise level in the measured r_{xx}. Furthermore, deviation from $r_{xx} = 0$ above a small threshold may occur for a gentle prebreakdown increase or for multiple-step transitions prior to abrupt breakdown [2,68]. For method B, I_c is simply given by the position of the r_{xx} maximum usually clear at the high-current tip of a transport diamond. Note that this corresponds to where the rise in V_{xx} with current is steepest. This is the most direct method to apply except if r_{xx} exhibits multiple-peak features or becomes unstable, which is sometimes the case, as noted in Sec. IV, for high electron density and high B field (low-filling factor) [68]. In general, the value of I_c determined by method A is smaller than that determined by method B; however, these methods can give similar values if breakdown is very abrupt.

Figure 6 shows the critical current I_c determined by method A [Fig. 6(a)] and method B [Fig. 6(b)] for even (E)- and odd (O)-integer filling factors for six electron densities in the range 1.6–3.9 $\times 10^{11}$ cm^{-2} [68]. For method A, since the noise level in r_{xx} near zero current for the largest transport diamonds is a few ohms, we have set the threshold value to be 10 Ω. From Fig. 6(a), for method A, we find that data points essentially fall on distinct common straight lines for even- and odd-filling factors. The common line for even-filling factors is steeper than that for odd-filling factors. The lines clearly do not extrapolate to the origin. The even- (odd-)filling-factor line intercepts zero current at ∼1.5 T (∼2.5 T). From Fig. 6(b), for method B, although the even- and odd-filling-factor families of lines are clear, there is considerably more variation and scatter than for method A, i.e., data points for different electron densities do not fall on a single common line. Even-filling-factor points above ∼1.5 T for each specific electron density appear to have approximately linear trends that would extrapolate to the origin, although there are deviations from the linear dependence near 1 T. Also, with increasing electron density, I_c for even-filling factors clearly changes more rapidly with B field. Although less pronounced, a similar behavior is observed too for the odd-filling-factor points. The odd-filling-factor trends intercept zero current near 1 T.

We make the following comments. First, the linear dependence with the B field for I_c data points determined by method A in Fig. 6(a) is, to a certain degree, unexpected. For GaAs/AlGaAs 2DEG heterostructures, it is often argued that the critical Hall electric field $E_c \propto I_c/\nu$ is proportional to $B^{3/2}$ (for example, see the discussion and plots of compiled data in Refs. [53,54] mostly extracted by method A). However, models for breakdown generally predict values for E_c that are larger than experimental values, and depend on factors such as the inclusion of higher-order tunneling processes, details of scattering (particularly the B-field dependence of the scattering rate), and Landau-level broadening induced by the Hall electric field [51,53]. Others have also suggested that a linear B dependence fit of compiled data appears to be at least as good as a $B^{3/2}$ dependence fit [67]. For our data, we do not find a power-law dependence for even- or odd-filling factors if we examine I_c/ν (data not shown). Consistent with our observations, we note that a linear dependence of the $\nu = 1$ and 2 breakdown currents with B field was also recently reported in Ref. [23] for InSb/AlInSb heterostructures with mobility exceeding ∼160 000 cm^2/Vs. To emphasize this point, data points for $\nu = 1$ and $\nu = 2$ are circled in Fig. 6(a). Second, the characteristics of I_c determined by method A [Fig. 6(a)] are notably different from the characteristics of I_c determined by method B [Fig. 6(b)], especially regarding the scatter of data points, i.e., method A data points appear to collapse onto two common lines but clearly method B data points do not. However, we stress that the two methods reflect two quite different features of Landau levels. Consistent with the discussion in Sec. V, we expect method A to be sensitive to how electrons tunnel between states in the tails of Landau levels (when the tunnel barrier for inter-Landau-level transitions becomes sufficiently transparent), and method B to be sensitive to how electrons tunnel resonantly between Landau levels at higher Hall electric field. Since in the framework of our simple picture for the transport diamonds method B offers a means to extract g factors for odd filling (crudely done for $\nu = 1$ in Sec. VI at $n = 1.9 \times 10^{11}$ cm^{-2}), we now examine this method more closely after introducing a simple procedure to account for the data scatter.

At first sight, the scatter in data points in Fig. 6(b) is counter to our intuition. In particular, based on our simple picture described in Sec. V, we take the individual I_c traces for even-integer filling in Fig. 6(b) to reflect the energy $\hbar\omega_c - |g_e^*|\mu_B B$ (see also Sec. VI). This energy is dominated by the cyclotron energy and is not expected to have any *significant* n dependence. However, this expectation neglects electrostatic details that determine the proportionality factor between current and energy. Since the Hall electric field is the dominant field and is proportional to I/n at fixed magnetic field, this prompted us to examine I_c/n instead of I_c (method B rescaled); see Fig. 6(c) in which *all* data points of Fig. 6(b) are replotted. Noticeable immediately, even-integer filling data points now effectively collapse onto a single (solid) line. This universal behavior means I_c is proportional not just to B, but also n, i.e., I_c/n and not I_c should be equated with energy $\hbar\omega_c - |g_e^*|\mu_B B$. Regarding the odd-integer filling data points, rescaling reduces the scatter to a degree and they lie in a region bounded by the dashed line (with steeper slope) and the dash-dotted line (with shallower slope) [69]. Interestingly, the order by slope of the rescaled odd-integer filling data point traces is inverted with respect to those prior to rescaling [see Fig. 6(b)]. The linear B-dependence trace now appears steepest (shallowest) for $n = 1.6 \times 10^{11}$ cm^{-2} ($n = 3.9 \times 10^{11}$ cm^{-2}), i.e., there is a trend for the slope to decrease with increasing n. Values of I_c estimated from the tips of the dark-blue colored $\nu = 1$ and $\nu = 2$ diamonds for

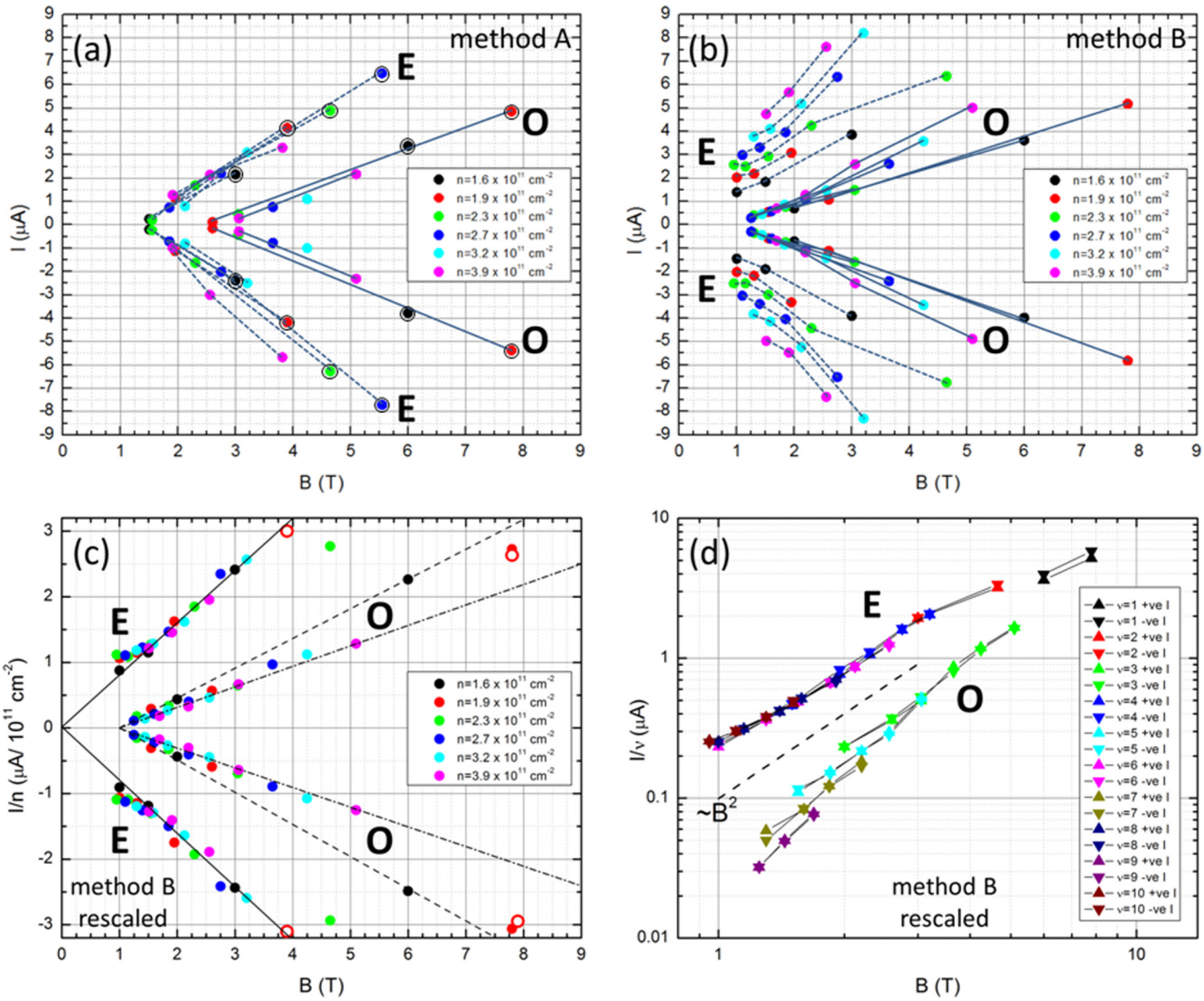

FIG. 6. Critical current I_c compiled for even (E)- and odd (O)-integer filling factors for electron densities in the range 1.6–3.9 $\times$ 10^{11} cm^{-2}. The values are determined by two methods on examination of $r_{xx}(I_{dc})$ traces that are used to build up the color maps in Fig. 3. In (a), I_c is the current at which r_{xx} exceeds 10 Ω (method A), and in (b), I_c is the current position of the r_{xx} maximum at the high-current tip of a transport diamond (method B). Guidelines are shown joining two or more data points for even- (dashed) or odd- (solid) integer filling factors at a given electron density. In (a), data points for $\nu = 1$ and $\nu = 2$ are circled. In (c), the data points from (b) are replotted to show I_c/n instead of I_c (method B rescaled). Even-integer filling data points effectively collapse onto a single (solid) line. Odd-integer filling data points lie in a region bounded by the dashed line (with steeper slope for $n = 1.6 \times 10^{11}$ cm^{-2} data points) and the dash-dotted line (with shallower slope for n 3.9×10^{11} cm^{-2} data points); see main text for further discussion. Although not strictly determined by method B, values of I_c estimated from the tips of the dark-blue colored $\nu = 1$ and $\nu = 2$ diamonds for $n = 1.9 \times 10^{11}$ cm^{-2} in Fig. 5 (see Sec. VI) and *rescaled* are also included (open red circles). In (d), the data points from (b) are replotted on a log-log scale and sorted by ν instead of n to show absolute values of I_c/ν (also effectively method B is rescaled since $\nu = nh/eB$). The dashed black line with a $\sim B^2$ dependence is included as a guide to the eye. In the legend, +ve I (−ve I) means positive (negative) current polarity.

$n = 1.9 \times 10^{11}$ cm^{-2} in Fig. 5 (see Sec. VI) and *rescaled* are also included in Fig. 6(c); see open red circles. Although not strictly determined by method B, since breakdown is fairly abrupt, these extra points nonetheless lie either very close to data points extracted by method B at the corresponding density, in the case of $\nu = 1$, or very close to the single common line for even-filling factor points, in the case of $\nu = 2$.

The rescaling procedure also implies that the critical Hall field E_c is proportional to B^2 when method B is applied since, empirically, $I_c \propto Bn$ ($E_c = hI_c/\nu e^2 w = BI_c/new$). To corroborate this, in Fig. 6(d) *all* data points of Fig. 6(b) are replotted on a log-log scale and sorted by ν instead of n to show absolute values of I_c/ν (also, effectively, method B rescaled). The dependence we see for both even and odd filling is closer to B^2 than B or $B^{3/2}$. Interestingly, this is similar to observations for Hall-induced resistance oscillations (HIROs) in high-mobility GaAs/AlGaAs 2DEGs at low magnetic fields (<0.5 T), where Zener tunneling between Landau levels takes place across distance $2R_c \sim 1/B$ (the

cyclotron diameter) [70]. If we equate the characteristic length scale δ for Zener tunneling introduced in Sec. VI to $2R_c$, this would lead to a B^2 dependence for E_c. However, in the strong quantum Hall regime at large magnetic fields, $2R_c$ is much smaller than the length of 1.6 μm at 3.9 T that we estimated earlier. We stress the rescaling in Fig. 6(c) and Fig. 6(d) involves no fitting or knowledge of quantities other than n or ν.

Having demonstrated that data points of I_c/n for even-integer filling collapse onto a single line which can be equated to the energy $\hbar\omega_c - |g_e^*|\mu_B B$, we proceed to estimate g factors for odd filling from Fig. 6(c). We now expect the individual I_c/n traces for odd-integer filling to be a measure of the energy $|g_o^*|\mu_B B$ (see also Secs. V and VI). By examining the ratio of the slopes of the single solid line for even filling and the dashed and dash-dotted bound lines for odd filling, we estimate $|g_o^*|$ to be in the range ∼15–21 if we take values of $0.047m_0$ and 4.8, respectively, for m^* and $|g_e^*|$. The value for the g factor appears to be larger for lower density [71]. In contrast to $|g_e^*|$, not only is a larger value for $|g_o^*|$ expected, but an n dependency is reasonable too. The increase of $|g_o^*|$ with decreasing n is significant and likely reflects an increase in the strength of the effective electron-electron interactions [63,65,72,73]. To investigate this point further, we end this section by comparing the effective exchange-enhanced g factors estimated for odd filling from the rescaled compiled data in Fig. 6(c) to those determined by conventional thermal-activation measurements over the same range of electron density.

At exact odd-integer filling, the Fermi level is midway between two broadened spin-split Landau subbands $(N,\uparrow)$ and $(N,\downarrow)$. Close to equilibrium ($I_{dc} = 0$ and small ac excitation current), the energy to activate electrons from the Fermi level to extended states in the broadened level $(N,\downarrow)$ is $E_{\rm gap}/2$, where $E_{\rm gap} = |g_o^*|\mu_B B - 2\Gamma$ (the effective energy gap between $(N,\uparrow)$ and $(N,\downarrow)$ [21,63–66,74–76]). This activation energy can be extracted from the temperature (T) dependence of r_{xx} at odd-filling-factor minima, namely, from an Arrhenius plot if $r_{xx} \sim \exp(-E_{\rm gap}/2k_BT)$, where k_B is the Boltzmann constant. We examined the temperature dependence of r_{xx} at $I_{dc} = 0$ for odd-filling-factor minima as a function of B. Plots of $\ln(r_{xx})$ vs $1/T$ for T in the range 0.3 to ∼1.6 K were found to be close to linear for $T \gtrsim 1$ K for electron densities in the range 1.6–3.9 × 10^{11} cm^{-2} (data not shown [34]). Fitting the plots at higher temperature where they are reasonably linear, $E_{\rm gap}$ was extracted. The values of $E_{\rm gap}$ are plotted in Fig. 7 as a function of B (B field at which the r_{xx} minima are located). From this plot, except for the lowest density, $|g_o^*|$ can be estimated from the linear dependence on B [77], while Γ can be estimated from the zero B-field intercept [65,74–76,78]. For n = 1.9, 2.3, 2.7, 3.2, and 3.9 × 10^{11} cm^{-2}, $|g_o^*|$ is determined to be 9.8, 9.7, 7.6, 7.1, and 5.9, respectively. The uncertainty in these numbers is estimated to be ±0.4. This number reflects uncertainty in the slopes of the fit lines for n = 2.7, 3.2, and 3.9 × 10^{11} cm^{-2} for which there are three data points in each case.

The trend of increasing $|g_o^*|$ with decreasing n suggested from the analysis of the rescaled method-B data in Fig. 6(c) is thus also seen in the thermal-activation data in Fig. 7. We note the similarity between our data in Fig. 7 with

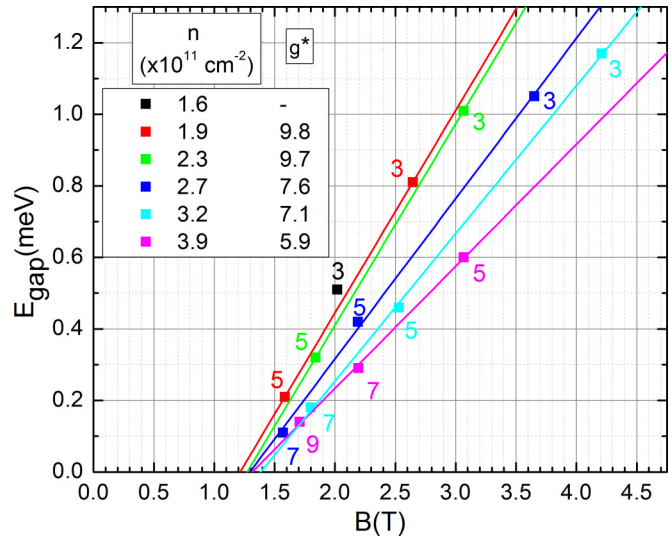

FIG. 7. Values of $E_{\rm gap}$ determined from the temperature dependence of r_{xx} at the ν = 3, 5, 7, and 9 minima ($I_{dc} = 0$) for different electron densities n as a function of B. The number next to a point identifies ν. The lines intercept the B axis in the range 1.2–1.4 T. Estimated values of $|g^*|$ from the slopes are also tabulated. There is no value shown for $n = 1.6 \times 10^{11}$ cm^{-2} since only one data point (for $\nu = 3$) could be extracted.

that in Ref. [65] for GaAs/AlGaAs 2DEGs: namely, for a given electron density, an energy gap for odd-filling factors ($\nu > 1$) extracted by thermal-activation measurements (for out-of-plane B field) which is approximately linear in the B field (and with a negative intercept at $B = 0$ reflecting the level broadening that is effectively constant), and an effective g factor determined from the slope that decreases with increasing n. The values of the exchange-enhanced g factor determined by thermal-activation measurements here are consistent with those extracted by the same technique and reported in earlier work for similar materials [21,66]. Notable, however, is that the estimated values for $|g_o^*|$ from the rescaled method-B approach are a factor of ∼2–3 times higher than those from the thermal-activation measurements [79]. Currently we do not have a fully detailed understanding of the difference. We believe some of the discrepancy may arise because the compared values were estimated for different density and filling-factor ranges, and Ref. [22] also reports a g factor for an In-based QW estimated by thermal activation that is lower than the value determined by other techniques; see note in Ref. [79]. A number of other factors may be relevant. For example, thermal-activation measurements are influenced by the Landau-level broadening which can vary to a degree with magnetic field. Furthermore, the exchange energy also depends on the difference in population of spin-up and spin-down subbands. Under certain conditions and dependent on details of disorder and spin-flip scattering, the spin polarization may not be at a maximum and this can impact the measured dependence of the spin gap [64,65,73,74]. Outside the scope of this paper, a more quantitative evaluation of the enhanced g factor requires involved self-consistent calculations for the density of states that depend on details of scattering mechanisms for InGaAs/InP QWs. Lastly, from

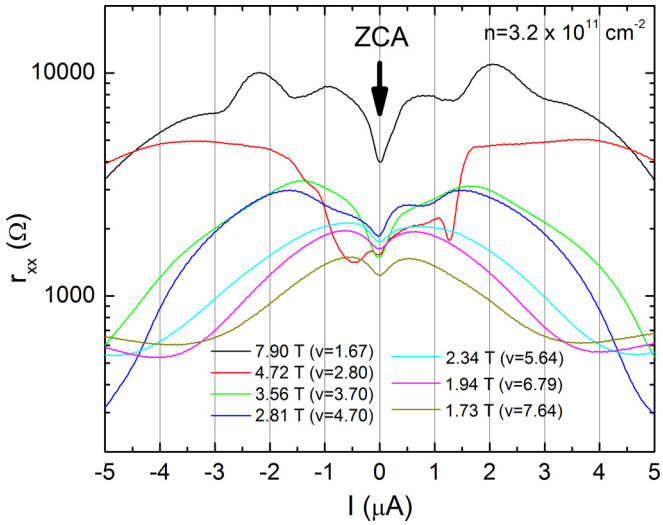

FIG. 8. r_{xx} sections through color map for B fields near where neighboring transport diamonds touch for electron density $n = 3.2 \times 10^{11}$ cm^{-2}. See r_{xx} color map in Fig. 3. The zero-current anomaly (ZCA) "dip" is labeled and is present in all traces shown.

the zero B-field intercepts in Fig. 7, we find 2Γ to be in the range ∼0.4–0.8 meV. These numbers are about a factor of 2 lower than those given in Sec. II that were determined by the more well-established Dingle plot method. Our estimation of Γ from analysis of Fig. 7 though neglects any contribution to conduction by mechanisms such as variable-range hopping [63,80] and assumes that the boundary in energy between localized and extended states in a density-of-states peak is well defined.

VIII. ZERO-CURRENT ANOMALY

Close inspection of the r_{xx} color maps in Fig. 3 reveals a narrow "dip" in r_{xx} in regions close to zero current, most notably where the transport diamonds touch. This dip is a signature of the zero-current anomaly (ZCA) described in Ref. [21]. In fact, the ZCA can be observed over a wide range of B field provided that r_{xx} is not zero in the vicinity of zero current over a current range exceeding ∼0.4 μA (see also Fig. 4). To illustrate this, Fig. 8 shows r_{xx} sections on a logarithmic scale for $n = 3.2 \times 10^{11}$ cm^{-2} that cut through the points close to where neighboring transport diamonds touch at zero current. At such points, encompassing the $\nu = 1$ to 8 transport diamonds, the ZCA is clear and has FWHM of typically ∼0.4 μA [81].

Studenikin *et al.* [21] described basic properties of the ZCA for InGaAs/InP Hall bars, but only for B fields up to ∼5 T and for an electron density ∼5.3×10^{11} cm^{-2}, so filling factors no lower than $\nu = 5$ were investigated. The ZCA FWHM was found to be ∼2.1 μA (∼0.25 μA) for a 100 -μm (10- μm)-wide Hall bar, so this indicates, consistent with the FWHM 0.4 μA for the 15- μm-wide Hall bar measured here, that the FWHM is proportional to the Hall bar width [82]. From the near linear increase in width of even-filling-factor transport diamonds with B field which principally reflects the growth in cyclotron energy (see discussion in Secs. V–VII), we can convert the FWHM of the ZCA into an energy set by $\hbar\omega_c - |g^*|\mu_B B$. For an effective mass of $0.047m_0$ and taking $|g_e^*| \sim 4.8$, we estimate that the FWHM ∼0.4 μA here is equivalent to an energy ∼0.3 meV.

Reference [21] also reported the ZCA in higher-mobility GaAs/AlGaAs Hall bar structures so the phenomenon appears to reflect intrinsic properties of a 2DEG. The origin of the ZCA is not understood and we are not aware of any theoretical description on this subject. In Ref. [21], it is speculated to originate from modifications to the density of states of interacting electrons in the presence of disorder and a magnetic field.

IX. CONCLUSIONS

We have investigated nonlinear magnetotransport in a Hall bar device made from a strained $In_{0.76}Ga_{0.24}As/In_{0.53}Ga_{0.47}As/InP$ quantum-well heterostructure (with mobility approaching 300 000 cm^2/Vs for $n \sim 4.0 \times 10^{11}$ cm^{-2} at 0.3 K). We have demonstrated that maps of the differential resistance (r_{xx} and r_{xy}) over a wide range of sheet current density (up to ∼1 A/m) and magnetic field (up to 9 T) provide a valuable insight into quantum Hall breakdown and a number of other nonlinear phenomena (including a spin-flip resonance at high current near $\nu = 1$, electric instability, phase inversion of SdH oscillations, and a zero-current anomaly). We have shown that these maps (phase diagrams) give detailed information about the conditions for and the energetics of quantum Hall breakdown. Compared to earlier work in Ref. [21], we extended our study to the strong quantum Hall regime (reaching filling factor $\nu = 1$). Also, an additional perspective was gained by incrementing the electron density in small steps by careful illumination and tracking the systematic evolution of the transport characteristics with n. We presented a simple picture for the principal features in the maps, namely, the distinctive transport diamonds and high-current protrusions (resonances) emerging from near the high-current tips of the $\nu = 1$ transport diamond, and introduced a simple tunneling model that qualitatively reproduces these features. Primary parameters such as critical current densities and critical Hall electric fields for $\nu = 1$ and 2, and an exchange-enhanced g factor for $\nu = 1$ were extracted. The critical Hall electric fields for the InGaAs/InP quantum well were found to be comparable to those reported for widely studied GaAs/AlGaAs 2DEG heterostructures.

A detailed examination was made of the B-field dependence of the critical current I_c as determined by two different methods and compiled for different values of n. From the first method (method A by which I_c is defined to be the current when r_{xx} exceeds a small threshold), we found I_c for both even ν and odd ν has an approximate linear dependence with the B field. This finding is similar to that for an investigation in another In-based quantum-well system [23], but does not fit with the often cited $B^{3/2}$ dependence for the critical Hall field E_c. From the second method (method B by which I_c is defined from the current position of the r_{xx} maxima at the tips of the transport diamonds), we found I_c for both even ν and odd ν also has an approximate linear dependence with the B field. While method B was easier to apply, there was (on initial inspection) seemingly more scatter in data points. However,

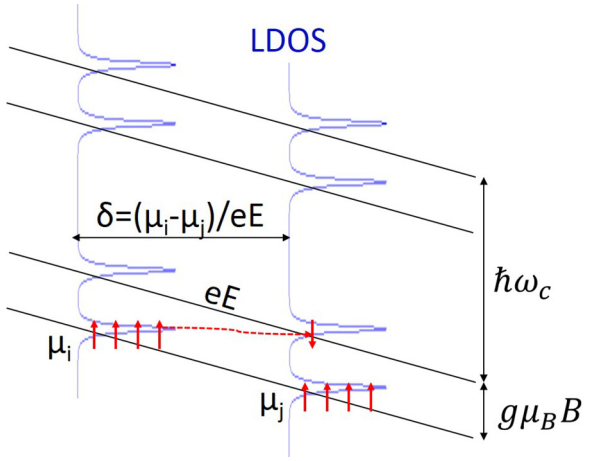

FIG. 9. The local density of states (LDOS) including disorder broadening in a quantizing magnetic field is shown in blue. A sufficiently large electric field E (typically the transverse Hall electric field across the Hall bar) will lead to a Zener tunneling transition between regions i and j separated by distance δ. Relevant for breakdown at $\nu = 1$, the dashed red arrow depicts the transition $(0,\uparrow) \rightarrow (0,\downarrow)$. The corresponding Landau levels are shifted in energy by $\mu_i - \mu_j$.

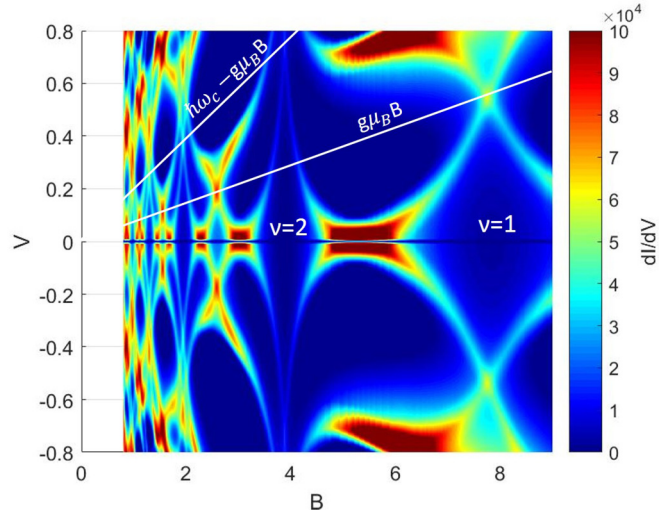

FIG. 10. Example of a color map of $\frac{dI}{dV}$ generated using expression (A2) with B in units of $4\nu^{-1}n$, taking $n = 1.9$ in units of 10^{11} cm^{-2} (compare the color map with the experimental color map in Fig. 5). We have set $\hbar\omega_c/g\mu_B B = 3.75$. This corresponds to $g \approx 11.5$: a value between g_e^* and g_o^* mentioned in Sec. VI. Since we have assumed a single value for the g factor, we have neglected many-body interaction effects. We also used $\Gamma_{\rm DOS} = \hbar\omega_c$ at 0.2 T, which is equivalent to ∼0.5 meV. V and dI/dV are in arbitrary units.

by simple rescaling, I_c/n data points for even ν were found to collapse onto a single curve. This universal behavior uncovered on rescaling even-ν data points also implies that E_c has a B^2 dependence when method B is applied. I_c/n data points for odd ν do not all collapse onto a single curve and we attributed this to signs that the exchange-enhanced g factor, g_o^* (a quantity that can be estimated from the slopes of the I_c/n traces for even and odd ν), increases with decreasing n. This trend was corroborated by examination of the effective energy gap for odd ν determined from conventional thermal-activation measurements. By method B, we estimated $|g_o^*|$ to be in the range ∼15–20 at base temperature.

We have demonstrated that building up a map of quantum Hall breakdown provides access to numerous nonlinear phenomena for carriers confined in two dimensions that are driven out of equilibrium. We have provided a perspective of the quantum Hall system from the quasiclassical regime at low magnetic field to the strong quantum Hall effect regime at high magnetic field by analyzing the entire phase diagram and presenting a step-by-step guide toward the different elements of that phase diagram. The measurement and analytical techniques we have described here can, in principle, be applied to any material hosting a two-dimensional electron or hole system. Furthermore, method B can complement existing techniques such as the coincidence technique [64] and the thermal-activation technique for estimation of exchange enhancement of spin splitting.

ACKNOWLEDGMENTS

Part of this work is supported by NSERC (Discovery Grant No. 208201) and INTRIQ.

APPENDIX: TUNNELING DENSITY-OF-STATES MODEL

Here we formulate a single-particle model describing the inter-Landau-level tunneling processes exemplified in Fig. 9.

We will assume that the system can be described by a simple tunneling Hamiltonian, which is given by the standard expression

$$I = \frac{e}{h}\sum_{ij} T_{ij} n_i (1 - n_j)\delta(\epsilon_j - \epsilon_i), \tag{A1}$$

where T_{ij} are the tunneling matrix elements. The local chemical potentials across the tunneling region are determined by the electric field E and the distance δ between i and j: $\mu_i = \mu + eE\delta/2$ and $\mu_j = \mu - eE\delta/2$. The uniform electric field in the model is governed by the dc bias, V, applied to the Hall bar (equivalent in the experiment to the dc current driven through the Hall bar, which causes the Landau levels to tilt across the Hall bar). For simplicity, we will assume $V = eE\delta$ and that the matrix elements T_{ij} do not depend on energy, which leads at zero temperature to

$$I(V) \sim \int_{\mu - eV/2}^{\mu + eV/2} d\epsilon D(\epsilon - eV/2) D(\epsilon + eV/2), \tag{A2}$$

where $D(\epsilon)$ is the LDOS of the broadened Landau levels. The broadened Landau levels are typically rounded close to the Landau-level energies (elliptic in the self-consistent Born approximation) with exponential tails between Landau levels. To mimic this behavior and in order to simulate the experimental findings, we assume the form of the Landau levels to be $e^{-|\epsilon/\Gamma_{\rm DOS}|^{2/3}}$ in the tails and $e^{-|\epsilon/\Gamma_{\rm DOS}|^{4/3}}$ close to the Landau levels ($\epsilon \simeq 0$), where ϵ is the energy relative to the center of a Landau level and $\Gamma_{\rm DOS}$ is the broadening. The qualitative features will depend on the particular choice of

Landau-level broadening. We tried different forms but chose one that reproduces well the main features observed.

The differential conductance is given by $g \sim dI/dV$. To apply this model to the four-terminal experimental configuration, we note that for large magnetic fields where $\sigma_{xx} < \sigma_{xy}$, $r_{xx} \simeq \sigma_{xx}/\sigma_{xy}^2$: here, σ_{ij} are the magnetoconductivity tensor elements. Hence we assume $r_{xx} \sim dI/dV$, using expression (A2), which we evaluate as a function of V and magnetic field. An example of a calculated r_{xx} color map is shown in Fig. 10. Although we do not expect our toy model to explain all aspects of the experimental r_{xx} color maps, it does nonetheless reproduce a number of key features: (i) transport diamonds that grow in size with B field and the alternating larger and smaller transport diamonds for even- and odd-filling factors, (ii) transport diamonds with clearly curved edges, and (iii) resonant features beyond the transport diamonds.

[1] K. von Klitzing, Annu. Rev. Condens. Matter Phys. **8**, 13 (2017).

[2] G. Ebert, K. von Klitzing, K. Ploog, and G. Weinmann, J. Phys. C **16**, 5441 (1983).

[3] G. Nachtwei, Physica E (Amsterdam) **4**, 79 (1999).

[4] M. Kawamura, H. Takahashi, K. Sugihara, S. Masubuchi, K. Hamaya, and T. Machida, Appl. Phys. Lett. **90**, 022102 (2007).

[5] M. Kawamura, K. Kono, Y. Hashimoto, S. Katsumoto, and T. Machida, Phys. Rev. B **83**, 041305 (2011).

[6] K. Ikushima, H. Sakuma, Y. Yoshimura, S. Komiyama, T. Ueda, and K. Hirakawa, Physica E (Amsterdam) **34**, 22 (2006).

[7] K. Ikushima, H. Sakuma, S. Komiyama, and K. Hirakawa, Phys. Rev. B **76**, 165323 (2007).

[8] L. Eaves, Physica B (Amsterdam) **298**, 1 (2001).

[9] L. Eaves, Physica E (Amsterdam) **9**, 45 (2001).

[10] J. C. Chen, Y. Tsai, Y. Lin, T. Ueda, and S. Komiyama, Phys. Rev. B **79**, 075308 (2009).

[11] C.-P. Lee, C. C. Chi, and J.-C. Chen, Phys. Rev. B **92**, 195410 (2015).

[12] S. Baer, C. Rössler, S. Hennel, H. C. Overweg, T. Ihn, K. Ensslin, C. Reichl, and W. Wegscheider, Phys. Rev. B **91**, 195414 (2015).

[13] A. V. Rossokhaty, Y. Baum, J. A. Folk, J. D. Watson, G. C. Gardner, and M. J. Manfra, Phys. Rev. Lett. **117**, 166805 (2016).

[14] S. Datta and B. Das, Appl. Phys. Lett. **56**, 665 (1990).

[15] J. Nitta, T. Akazaki, H. Takayanagi, and T. Enoki, Phys. Rev. Lett. **78**, 1335 (1997).

[16] I. Žutić, J. Fabian, and S. Das Sarma, Rev. Mod. Phys. **76**, 323 (2004).

[17] Y. Hirayama, G. Yusa, K. Hashimoto, N. Kumada, T. Ota, and K. Muraki, Semicond. Sci. Technol. **24**, 023001 (2009).

[18] M. Kohda, S. Nakamura, Y. Nishihara, K. Kobayashi, T. Ono, J.-i. Ohe, Y. Tokura, T. Mineno, and J. Nitta, Nat. Commun. **3**, 1082 (2012).

[19] J. Shabani, M. Kjaergaard, H. J. Suominen, Y. Kim, F. Nichele, K. Pakrouski, T. Stankevic, R. M. Lutchyn, P. Krogstrup, R. Feidenhans'l, S. Kraemer, C. Nayak, M. Troyer, C. M. Marcus, and C. J. Palmstrøm, Phys. Rev. B **93**, 155402 (2016).

[20] M. Kohda and G. Salis, Semicond. Sci. Technol. **32**, 073002 (2017).

[21] S. A. Studenikin, G. Granger, A. Kam, A. S. Sachrajda, Z. R. Wasilewski, and P. J. Poole, Phys. Rev. B **86**, 115309 (2012).

[22] G. Nachtwei, A. Manolescu, N. Nestle, and H. Künzel, Phys. Rev. B **63**, 045306 (2000).

[23] J. A. Alexander-Webber, A. M. R. Baker, P. D. Buckle, T. Ashley, and R. J. Nicholas, Phys. Rev. B **86**, 045404 (2012).

[24] H. Hardtdegen, R. Meyer, M. Hollfelder, T. Schäpers, J. Appenzeller, H. Løken-Larsen, T. Klocke, C. Dieker, B. Lengeler, H. Lüth, and W. Jäger, J. Appl. Phys. **73**, 4489 (1993).

[25] A. Chin and T. Y. Chang, J. Vac. Sci. Technol. B **8**, 364 (1990).

[26] H. Hardtdegen, R. Meyer, H. Løken-Larsen, J. Appenzeller, T. Schäpers, and H. Lüth, J. Cryst. Growth **116**, 521 (1992).

[27] P. Ramvall, N. Carlsson, P. Omling, L. Samuelson, W. Seifert, Q. Wang, K. Ishibashi, and Y. Aoyagi, J. Appl. Phys. **84**, 2112 (1998).

[28] S. Gozu, T. Kita, Y. Sato, S. Yamada, and M. Tomizawa, J. Cryst. Growth **227-228**, 155 (2001).

[29] S. A. Studenikin, P. T. Coleridge, P. Poole, and A. Sachrajda, JETP Lett. **77**, 311 (2003).

[30] W. Desrat, F. Giazotto, V. Pellegrini, F. Beltram, F. Capotondi, G. Biasiol, L. Sorba, and D. K. Maude, Phys. Rev. B **69**, 245324 (2004).

[31] D. Ercolani, G. Biasiol, E. Cancellieri, M. Rosini, C. Jacoboni, F. Carillo, S. Heun, L. Sorba, and F. Nolting, Phys. Rev. B **77**, 235307 (2008).

[32] F. Herzog, C. Heyn, H. Hardtdegen, T. Schäpers, and D. Grundler, Appl. Phys. Lett. **107**, 092101 (2015).

[33] C. Chen, I. Farrer, S. Holmes, F. Sfigakis, M. Fletcher, H. Beere, and D. Ritchie, J. Cryst. Growth **425**, 70 (2015).

[34] V. Yu, Ph.D. thesis, McGill University, 2017, http://digitool.library.mcgill.ca/webclient/DeliveryManager?pid=148260&custom_att_2=direct.

[35] S. Das Sarma and E. H. Hwang, Phys. Rev. B **90**, 035425 (2014).

[36] For the fit calculation, the Bohr radius, effective mass, and static dielectric constant are, respectively, set to 17 nm, $0.047m_0$ (m_0 is the free-electron mass), and 15. The Si-doped InP layer above the QW is 5 nm wide and nominally doped to 6.7×10^{17} cm^{-3} so we set $n_i = 3.35 \times 10^{11}$ cm^{-2}, where n_i is the effective 2D density of the remote ionized impurities (we assume the donors are fully ionized). The setback distance is set to 42.5 nm (this is the distance from the middle of the 10-nm-wide $In_{0.76}Ga_{0.24}As$ channel to the middle of the Si-doped InP layer). Fit parameters are $\mu_A = 349\,000 \pm 7000$ cm^2/Vs, and $n_B = (1.8 \pm 0.2) \times 10^{15}$ cm^{-3}, where n_B is the effective density of the background ionized impurities. The value for n_B is in line with expectations for the chemical beam epitaxy system used to grow the heterostructure.

[37] M. J. Kane, D. A. Anderson, L. L. Taylor, and S. J. Bass, J. Appl. Phys. **60**, 657 (1986).

[38] A. Gold, Phys. Rev. B **38**, 10798 (1988).

[39] J. A. Brum and G. Bastard, Solid State Commun. **53**, 727 (1985).

[40] G. Bastard, Appl. Phys. Lett. **43**, 591 (1983).

[41] P. T. Coleridge, Phys. Rev. B **44**, 3793 (1991).

[42] J. Q. Zhang, S. Vitkalov, and A. A. Bykov, Phys. Rev. B **80**, 045310 (2009).

[43] K. Panos, R. R. Gerhardts, J. Weis, and K. von Klitzing, New J. Phys. **16**, 113071 (2014).

[44] We have also examined the color maps of r_{xx} replotted with $1/B$ on the x axis rather than B (data not shown [34]). The diamond center positions are now periodic in $1/B$ as expected, but the edges of the low-filling-factor diamonds are still curved after the transformation. Other reports also show that the decrease of the critical current with B field on moving away from the maximum critical current is not linear (see, for example, Refs. [54,2]).

[45] V. Yu, M. Hilke, P. Poole, S. Studenikin, and D. G. Austing (unpublished).

[46] R. R. Du, H. L. Stormer, D. C. Tsui, L. N. Pfeiffer, and K. W. West, Phys. Rev. Lett. **70**, 2944 (1993).

[47] A. M. Chang, M. A. Paalanen, D. C. Tsui, H. L. Störmer, and J. C. M. Hwang, Phys. Rev. B **28**, 6133 (1983).

[48] The theoretical energy gap for fractions is given by $\Delta_{\rm th} = Ce^2/4\pi\varepsilon\ell_B$, where C depends on the filling factor and the details of the theory (typically $0.01 < C < 0.1$), ε is the static dielectric constant, and ℓ_B is the magnetic length. From experimental data for the energy gap for fractional states $\Delta_{\rm exp} = \Delta_{\rm th} - \Gamma$ shown in Ref. [46] for GaAs ($\varepsilon = 13$), we first estimate $C = 0.075$. Using this C for InGaAs and taking $\varepsilon = 15$, we evaluate $\Delta_{\rm th} = 0.56$ meV (0.74 meV) at 4 T (7 T).

[49] N. Deng, G. C. Gardner, S. Mondal, E. Kleinbaum, M. J. Manfra, and G. A. Csáthy, Phys. Rev. Lett. **112**, 116804 (2014).

[50] L. Eaves and F. W. Sheard, Semicond. Sci. Technol. **1**, 346 (1986).

[51] S. Komiyama and Y. Kawaguchi, Phys. Rev. B **61**, 2014 (2000).

[52] Note that the point where the $\nu = 1$ and $\nu = 2$ diamonds touch [in Fig. 5(b)] is not at $\nu = 1.5$ but $\nu > 1.5$.

[53] S. Kawaji, Semicond. Sci. Technol. **11**, 1546 (1996).

[54] B. Jeckelmann and B. Jeanneret, Rep. Prog. Phys. **64**, 1603 (2001).

[55] From thermal-activation measurements in a ^{4}He cryostat on a second Hall bar device made from a similar $In_{0.76}Ga_{0.24}As/In_{0.53}Ga_{0.47}As/InP$ heterostructure with $n = 1.5 \times 10^{11}$ cm^{-2} (data not shown [34]), g^* at $\nu = 2$ was estimated. For an effective electron mass $m^* = 0.047m_0$ and Landau-level broadening $\Gamma \sim 1$ meV (see Sec. II), we evaluated $|g^*|$ to be 4.8 ± 0.9. This value is consistent with the theoretical estimate of 5.45 for the bare g factor from the non-self-consistent calculation cited in Ref. [21]. The effective g factor here for the spin-unpolarized $\nu = 2$ state is not subject to strong enhancement by many-body electron-electron exchange interactions so is lower than the values of g^* determined later in Secs. VI and VII at odd-filling factors (see also Ref. [66]).

[56] R. J. Haug, Semicond. Sci. Technol. **8**, 131 (1993).

[57] J. Weis and K. von Klitzing, Philos. Trans. R. Soc. London A **369**, 3954 (2011).

[58] T. Sanuki, K. Oto, S. Takaoka, K. Murase, and K. Gamo, Solid State Commun. **117**, 343 (2001).

[59] J. Hayakawa, K. Muraki, and G. Yusa, Nat. Nanotechnol. **8**, 31 (2012).

[60] In Ref. [9], an estimate is made for the characteristic energy (the length scale corresponding to Landau-level wave-function overlap) of a simple model potential representing a nearby ionized impurity sufficient to create a locally enhanced electric field to explain certain features of breakdown in the region of $\nu = 2$ of the device studied when the *average* Hall electric field is relatively small (with value ~7 kV/m, which is small compared to that theoretically expected for inter-Landau-level tunneling between uniformly tilted levels). The value for the characteristic energy (length scale) was estimated to be a few millielectronvolts (comparable to the magnetic field length). Our deduction given in Sec. II that the effective random potential fluctuation in the InGaAs QW studied has amplitude ~2 meV fits in with the picture that locally enhanced electrical fields are naturally present and are an important factor.

[61] A percolation picture of the breakdown in Ref. [83] examines theoretically the abrupt formation of metallic conduction filaments across the Hall bar. The model requires the presence of regions in the Hall bar with locally enhanced electric fields induced in the calculations by a disorder potential to generate unstable energy-occupation configurations. In this work, only $\nu = 2$ is considered and the calculated values for the critical electric field are still larger than typically measured experimental values.

[62] There is still no complete consensus on the quantum Hall breakdown mechanism. References [53,67] include interesting extended commentaries on whether leading models for breakdown can be reconciled and describe the considerable challenges in interpreting available experimental data with these models given the wide variety of Hall bars studied (with different Hall bar layouts, channel widths, channel lengths, and mobilities). We note that under the assumption of a uniform Hall electric field, application of the Zener tunneling mechanism even for well-studied GaAs/AlGaAs structures, with commonly reported breakdown electric fields (such as those tabulated in Ref. [53]), would give a characteristic length δ of the order of a micron at 4 T. Explicitly, from the compilation of data in Refs. [53,54], the *average* breakdown electric field is typically in the range 2–6 kV/m at 4 T for even-filling factors, which corresponds to δ in the range 1.1–3.4 μm for a cyclotron energy of ~1.7 meV/T relevant to a GaAs QW: these δ values are significantly larger than the corresponding magnetic field length ~13 nm. The value of δ estimated for the InGaAs QW studied is therefore similar to that for GaAs/AlGaAs structures. Beyond the likely important role of locally enhanced electric fields near the Hall bar edges and random potential fluctuations, Ref. [53] discusses the possible influence of higher-order tunneling processes, and Landau-level broadening induced by the Hall electric field. Even with the widely cited bootstrap-type electron heating model of Komiyama and Kawaguchi [51], which incorporates Zener tunneling as a component, the predicted breakdown Hall electric fields still exceed those experimentally measured (see Fig. 6 in Ref. [51]). This model is subject to assumptions about the energy-relaxation mechanism (presumed to be dominated by intra-Landau-level acoustic-phonon scattering) and uncertainty in parameters. Lastly, in most detailed descriptions and discussions of breakdown mechanisms, only breakdown at even-filling factor is considered (Ref. [53] is one exception).

[63] T. Ando, A. B. Fowler, and F. Stern, Rev. Mod. Phys. **54**, 437 (1982).

[64] R. J. Nicholas, R. J. Haug, K. v. Klitzing, and G. Weimann, Phys. Rev. B **37**, 1294 (1988).

[65] D. R. Leadley, R. J. Nicholas, J. J. Harris, and C. T. Foxon, Phys. Rev. B **58**, 13036 (1998).

[66] S. S. Krishtopenko, K. V. Maremyanin, K. P. Kalinin, K. E. Spirin, V. I. Gavrilenko, N. V. Baidus, and B. N. Zvonkov, Semiconductors **49**, 191 (2015).

[67] O. Makarovsky, A. Neumann, L. Dickinson, L. Eaves, P. Main, M. Henini, S. Thoms, and C. Wilkinson, Physica E (Amsterdam) **12**, 178 (2002).

[68] For method A, generally data points for even ν could be extracted above ∼1.5 T; however, above 6 T, determination for $\nu = 2$ was not straightforward because of fluctuations or multiple-step transitions prior to abrupt breakdown when $n > 2.7 \times 10^{11}$ cm^{-2}. For odd ν, other than for $\nu = 1$ which moved out of range when $n > 1.9 \times 10^{11}$ cm^{-2}, only data points for $\nu = 3$ could be extracted over a wide range of n. For method B, more data points could be extracted and this was generally straightforward above ∼1 T. However, for even ν, determination was not possible or straightforward if the transport diamond width was close to or exceeded the current sweep range (for example, $\nu = 2$ at $n = 1.9 \times 10^{11}$ cm^{-2}), or multiple-peak features developed at breakdown (for example, $\nu = 2$ at $n = 2.3 \times 10^{11}$ cm^{-2}; note that the data points for this density fall short of the common lines in the lower two panels of Fig. 6 for even-filling-factor points after rescaling), or widespread instability occurred beyond breakdown ($\nu = 2$ beyond ∼5 T for $n > 2.3 \times 10^{11}$ cm^{-2}).

[69] In Figs. 6(c) and 6(d), even after rescaling, there is more scatter in odd-integer filling data points than for even-integer filling-factor points. As discussed in Sec. VII, not only can this be a sign of an exchange-enhanced g factor that varies with n, but also of an exchange-enhanced g factor that varies with B field at constant n.

[70] C. L. Yang, J. Zhang, R. R. Du, J. A. Simmons, and J. L. Reno, Phys. Rev. Lett. **89**, 076801 (2002).

[71] For $n = 1.9 \times 10^{11}$ cm^{-2}, the estimate of $|g_o^*|$ for $\nu = 1$ from the slopes of the lines in Fig. 6(c) is higher than the crude estimate of $|g_o^*|$ for $\nu = 1$ given in Sec. VI. For that estimate, however, Landau-level broadening was neglected and so the $|g_o^*|\mu_B B$ line bounding odd-ν diamonds was assumed to extrapolate to the origin (see Fig. 5). However, Fig. 6(c) reveals that odd-ν data points generally lie on lines that do not extrapolate to the origin, but instead intercept zero current near 1 T. As a consequence, the slope and hence the extracted g factor will be larger.

[72] Y. G. Sadofyev, A. Ramamoorthy, B. Naser, J. P. Bird, S. R. Johnson, and Y.-H. Zhang, Appl. Phys. Lett. **81**, 1833 (2002).

[73] B. Nedniyom, R. J. Nicholas, M. T. Emeny, L. Buckle, A. M. Gilbertson, P. D. Buckle, and T. Ashley, Phys. Rev. B **80**, 125328 (2009).

[74] A. Usher, R. J. Nicholas, J. J. Harris, and C. T. Foxon, Phys. Rev. B **41**, 1129 (1990).

[75] Y. Zhang, Z. Jiang, J. P. Small, M. S. Purewal, Y.-W. Tan, M. Fazlollahi, J. D. Chudow, J. A. Jaszczak, H. L. Stormer, and P. Kim, Phys. Rev. Lett. **96**, 136806 (2006).

[76] L. Li, F. Yang, G. J. Ye, Z. Zhang, Z. Zhu, W. Lou, X. Zhou, L. Li, K. Watanabe, T. Taniguchi, K. Chang, Y. Wang, X. H. Chen, and Y. Zhang, Nat. Nanotechnol. **11**, 593 (2016).

[77] We assume $|g_o^*|$ does not vary with odd ν at fixed electron density. This is reasonable since we analyze $\nu = 3$, 5, 7, and 9 and not $\nu = 1$ (where exchange can be more strongly enhanced). The calculations in Ref. [66] show some weak dependence of the exchange-enhanced g factor as a function of odd ν.

[78] V. T. Dolgopolov, A. A. Shashkin, A. V. Aristov, D. Schmerek, W. Hansen, J. P. Kotthaus, and M. Holland, Phys. Rev. Lett. **79**, 729 (1997).

[79] We note that the g factors we estimate from thermal-activation measurements are determined with data points for odd-filling factors no lower than $\nu = 3$ with electron densities greater than 1.6×10^{11} cm^{-2} (see Fig. 7), whereas the upper limit for the g factors estimated from the transport diamonds principally reflects the width of the $\nu = 1$ transport diamond at the lowest electron density (see Fig. 6) where the exchange enhancement is expected to be largest. See, also, Refs. [73,77]. Interestingly, Nachtwei *et al.* [22] report a g factor determined by thermal activation for $\nu = 1$ in an InGaAs/InAlAs QW that was significantly lower (by factor ∼4) than the g factor found by another technique.

[80] A. Buss, F. Hohls, F. Schulze-Wischeler, C. Stellmach, G. Hein, R. J. Haug, and G. Nachtwei, Phys. Rev. B **71**, 195319 (2005).

[81] The FWHM value of ∼0.4 μA is a typical value for the selected sections shown in Fig. 8. Examination of other sections near where neighboring transport diamonds touch gives values for the FWHM as low as 0.2 μA.

[82] In Ref. [21], it is erroneously stated that the ZCA width is inversely proportional to the Hall bar width.

[83] V. Tsemekhman, K. Tsemekhman, C. Wexler, J. H. Han, and D. J. Thouless, Phys. Rev. B **55**, R10201(R) (1997).